



Article

# Solid-State Construction of $\text{CuO}_x/\text{Cu}_{1.5}\text{Mn}_{1.5}\text{O}_4$ Nanocomposite with Abundant Surface $\text{CuO}_x$ Species and Oxygen Vacancies to Promote CO Oxidation Activity

Baolin Liu <sup>1,2,†</sup>, Hao Wu <sup>3,†</sup>, Shihao Li <sup>3</sup>, Mengjiao Xu <sup>2</sup>, Yali Cao <sup>2,\*</sup> and Yizhao Li <sup>1,3,\*</sup> 

<sup>1</sup> Yangtze Delta Region Institute (Huzhou), University of Electronic Science and Technology of China, Huzhou 313001, China; liubaolin6977@163.com

<sup>2</sup> State Key Laboratory of Chemistry and Utilization of Carbon Based Energy Resources, College of Chemistry, Xinjiang University, Urumqi 830017, China; xmj\_1117@163.com

<sup>3</sup> College of Chemical Engineering, Xinjiang University, Urumqi 830046, China; wuhaode123@eyou.com (H.W.); lsh1531@126.com (S.L.)

\* Correspondence: caoyali@xju.edu.cn (Y.C.); yizhao@csj.uestc.edu.cn (Y.L.); Tel./Fax: +86-572-2370780 (Y.L.)

† These authors contributed equally to this work.

**Abstract:** Carbon monoxide (CO) oxidation performance heavily depends on the surface-active species and the oxygen vacancies of nanocomposites. Herein, the  $\text{CuO}_x/\text{Cu}_{1.5}\text{Mn}_{1.5}\text{O}_4$  were fabricated via solid-state strategy. It is manifested that the construction of  $\text{CuO}_x/\text{Cu}_{1.5}\text{Mn}_{1.5}\text{O}_4$  nanocomposite can produce abundant surface  $\text{CuO}_x$  species and a number of oxygen vacancies, resulting in substantially enhanced CO oxidation activity. The CO is completely converted to carbon dioxide ( $\text{CO}_2$ ) at 75 °C when  $\text{CuO}_x/\text{Cu}_{1.5}\text{Mn}_{1.5}\text{O}_4$  nanocomposites were involved, which is higher than individual  $\text{CuO}_x$ ,  $\text{MnO}_x$ , and  $\text{Cu}_{1.5}\text{Mn}_{1.5}\text{O}_4$ . Density function theory (DFT) calculations suggest that CO and  $\text{O}_2$  are adsorbed on  $\text{CuO}_x/\text{Cu}_{1.5}\text{Mn}_{1.5}\text{O}_4$  surface with relatively optimal adsorption energy, which is more beneficial for CO oxidation activity. This work presents an effective way to prepare heterogeneous metal oxides with promising application in catalysis.

**Keywords:** solid-state synthesis;  $\text{CuO}_x/\text{Cu}_{1.5}\text{Mn}_{1.5}\text{O}_4$  nanocomposites; surface  $\text{CuO}_x$  species; oxygen vacancies; CO oxidation



**Citation:** Liu, B.; Wu, H.; Li, S.; Xu, M.; Cao, Y.; Li, Y. Solid-State Construction of  $\text{CuO}_x/\text{Cu}_{1.5}\text{Mn}_{1.5}\text{O}_4$  Nanocomposite with Abundant Surface  $\text{CuO}_x$  Species and Oxygen Vacancies to Promote CO Oxidation Activity. *Int. J. Mol. Sci.* **2022**, *23*, 6856. <https://doi.org/10.3390/ijms23126856>

Academic Editor: Shaodong Zhou

Received: 21 May 2022

Accepted: 18 June 2022

Published: 20 June 2022

**Publisher's Note:** MDPI stays neutral with regard to jurisdictional claims in published maps and institutional affiliations.



**Copyright:** © 2022 by the authors. Licensee MDPI, Basel, Switzerland. This article is an open access article distributed under the terms and conditions of the Creative Commons Attribution (CC BY) license (<https://creativecommons.org/licenses/by/4.0/>).

## 1. Introduction

Transition metal oxide catalysts for eliminating carbon monoxide (CO) at lower temperatures have attracted enormous attention in the past decades for their inexpensive cost and wide applications in catalytic applications and environmental protection [1–3]. Many techniques, such as morphology control [4–7], engineering defects [8–10], and construction of composite oxides [11–13] have been developed to improve the CO oxidation performance of transition metal oxide catalysts. Particularly, heterogeneous metal oxides that have exhibited excellent performances in CO oxidation fields [14–16] are the most widely studied because of their interactions of components [17]. Previous works have gradually demonstrated that heterogeneous metal oxides with synergistic interactions between two components are crucial for promoting catalytic performances [12,18,19]. The catalytic activity of nanocomposites depends significantly on surface active species and oxygen vacancies [20]. Therefore, the manipulation of the surface-active species and the oxygen vacancies of nanocomposites by simple strategy to optimize their catalytic performance is of great importance to meet the application in practice.

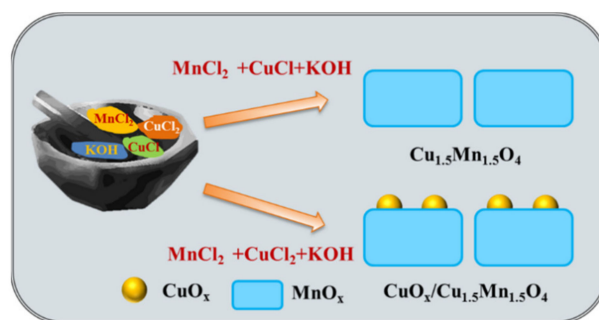
In the past few decades, many transition metal oxide catalysts have been developed, mainly including  $\text{CeO}_2$  [13,21,22],  $\text{MnO}_2$  [23–25],  $\text{Co}_3\text{O}_4$  [26–28],  $\text{CuO}$  [29–31],  $\text{Fe}_2\text{O}_3$  [32–34] et al.,  $\text{Co}_3\text{O}_4\text{-CeO}_{2-x}$  [16,35], Cu-Mn [36], Ce-Cu [37,38], and Ce-Mn [39,40] composite oxides. Different active metals and carriers will result in different interactions

between metals and carriers and different exposed active sites, thus making them have different reactivity for CO catalytic oxidation. Yu [16] synthesized the catalyst of  $\text{Co}_3\text{O}_4\text{-CeO}_2$  nanocomposite, which showed good catalytic activity due to its special hollow multishell structure and the interaction between the two components. Chen [41] constructed  $\text{CuO}_x\text{-CeO}_2$  nanorods and explained the relationship between reduction treatment and catalytic activity, indicating that reduction treatment accelerates the generation of active sites. In our previous works, we fabricated a  $\text{CuO}_x\text{-CeO}_2$  catalyst via the solid-state method [22], and investigated the influence of heating rate on catalytic performance. It was demonstrated that the heating rate can regulate the surface dispersion of  $\text{CuO}_x$  on  $\text{CeO}_2$  surface, resulting in enhanced catalytic performance. Copper-manganese mixed oxide catalyst is a typical transition metal-based catalyst in the CO oxidation reaction, which is known for its high activity at high temperature and low cost [36,42]. However, current commercial copper-manganese catalysts exhibit relatively low catalytic activity at low temperatures for CO oxidation. Furthermore, specific deactivation frequently occurs during the catalytic process [43,44]. The catalytic performance of heterogeneous catalysts is closely associated with their synergistic interactions and oxygen vacancies. In addition, many controllable synthetic strategies, such as direct calcination [30] and hydrothermal/solvothermal synthesis [45,46], have been developed for the fabrication of heterogeneous catalysts with the active two-phase interface, controllable size, shape, and composition in view of the purpose of improving catalytic performance. These synthetic routes are usually low-producing, time-consuming, and high-energy-consuming [47,48]. Solid-state synthesis integrated the advantages of low cost, eco-friendly and large-scale and have aroused wide concern in recent years [49–53].

Herein, a solid-state synthesis was developed to fabricate the  $\text{CuO}_x/\text{Cu}_{1.5}\text{Mn}_{1.5}\text{O}_4$ , which was implemented by the straightforward grinding of copper salt, manganese salt, and potassium hydroxide at ambient conditions. The metal oxide catalysts fabricated by solid-state synthesis are considered a simple and economical approach because they are without complicated procedures and organic solvents. The as-prepared  $\text{CuO}_x/\text{Cu}_{1.5}\text{Mn}_{1.5}\text{O}_4$  exhibit significant advantages compared to other methods. The catalytic performance was obviously promoted, which can be attributed to the surface  $\text{CuO}_x$  species and the number of oxygen vacancies. More importantly, this work presents us with an effective way to prepare heterogeneous metal oxides with outstanding catalytic performance.

## 2. Results and Discussion

The preparation process of  $\text{CuO}_x/\text{Cu}_{1.5}\text{Mn}_{1.5}\text{O}_4$  is schematically illustrated in Scheme 1. The  $\text{CuO}_x/\text{Cu}_{1.5}\text{Mn}_{1.5}\text{O}_4$  can be efficiently synthesized by the solvent-free strategy. The corresponding X-ray powder diffraction (XRD) patterns of  $\text{CuO}_x/\text{Cu}_{1.5}\text{Mn}_{1.5}\text{O}_4$  are exhibited in Figure 1. The peaks detected at  $2\theta = 18.55, 30.51, 35.94, 37.60, 43.69, 54.23, 57.81,$  and  $63.51$  degrees were indexed to  $\text{Cu}_{1.5}\text{Mn}_{1.5}\text{O}_4$  spinel solid solution (JCPDS No:70-0262). The diffraction peak at  $38.92$  degrees attributes to the isolated  $\text{CuO}$  phases. These results demonstrate the successful synthesis of  $\text{CuO}_x/\text{Cu}_{1.5}\text{Mn}_{1.5}\text{O}_4$  nanocomposites by solid-state strategy. As shown in Figure 1b, compared with individual  $\text{CuO}$  species, the major diffraction peaks of the products with different Cu/Mn mole ratios were slightly shifted to a higher degree, which can be ascribed to the change of the lattice parameters. In addition, XRD patterns show the characteristic peaks of  $\text{CuO}$  and  $\text{MnO}_x$ , as shown in Figure S1. The ratios of  $\text{Cu}^{2+}/\text{Cu}^+$  in  $\text{Cu}_2\text{O}/\text{CuO}$  can be controlled by adjusting the types of copper salts. The energy-dispersive X-ray spectrum (EDS) mapping analyses was implemented to identify the elementary composition of the  $\text{CuO}_x/\text{Cu}_{1.5}\text{Mn}_{1.5}\text{O}_4$ . The Cu/Mn molar ratio in the as-prepared samples is close to 1.0 (Figure S2), which has no significant difference compared to the theoretical value during synthesis.



**Scheme 1.** Schematic illustration of the construction of  $\text{CuO}_x/\text{Cu}_{1.5}\text{Mn}_{1.5}\text{O}_4$  nanocomposite with different surface  $\text{CuO}_x$  species.

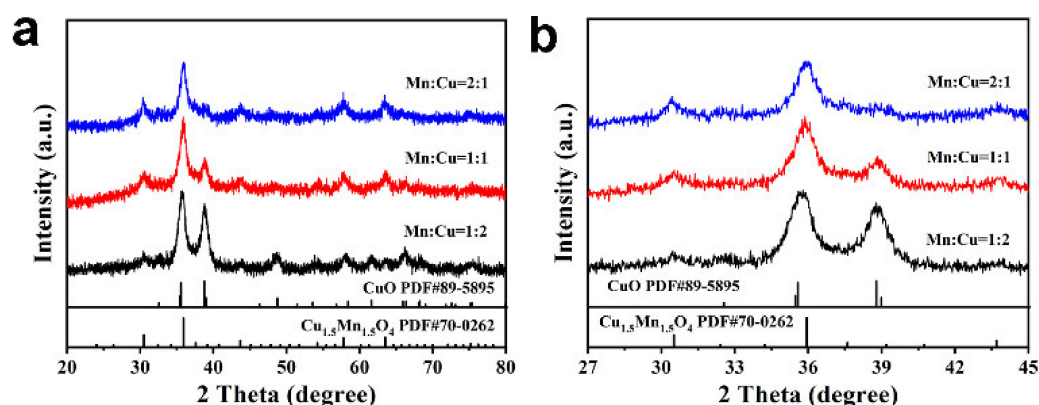


**Figure 1.** (a) The powder XRD patterns of  $\text{CuO}_x/\text{Cu}_{1.5}\text{Mn}_{1.5}\text{O}_4$ ; (b) partially enlarged profiles.

The scanning electron microscope (SEM) and transmission electron microscopes (TEM) images as shown in Figure 2 further prove that the nanoparticles with 11–16 nm (Figure 2e) existed in  $\text{CuO}_x/\text{Cu}_{1.5}\text{Mn}_{1.5}\text{O}_4$ . Additionally, the interplanar spacing of 0.250 nm and 0.232 nm, revealed by the high-resolution transmission electron microscopes (HRTEM) image (Figure 2i), correspond to (311) and (111) planes of  $\text{Cu}_{1.5}\text{Mn}_{1.5}\text{O}_4$  and CuO, respectively. The element mapping results are exhibited in Figure 2, confirming that the Cu and Mn elements are uniformly dispersed on the surface of  $\text{CuO}_x/\text{Cu}_{1.5}\text{Mn}_{1.5}\text{O}_4$ . These results further confirm the successful synthesis of  $\text{CuO}_x/\text{Cu}_{1.5}\text{Mn}_{1.5}\text{O}_4$  by solid-state strategy. Furthermore, the morphologies of  $\text{CuO}_x/\text{Cu}_{1.5}\text{Mn}_{1.5}\text{O}_4$  prepared by adjusting the molar ratios of Cu/Mn were also acquired (Figure S3), displaying agglomerated nanoparticles. The morphologies of CuO,  $\text{Cu}_2\text{O}$ -CuO, and  $\text{MnO}_x$  are shown in Figures S4–S6, which also exhibit irregular nanoparticles.

The CO catalytic performance of the as-obtained  $\text{CuO}_x/\text{Cu}_{1.5}\text{Mn}_{1.5}\text{O}_4$  were firstly evaluated. As shown in Figure S7a,b, the best CO catalytic activity is  $\text{CuO}_x/\text{Cu}_{1.5}\text{Mn}_{1.5}\text{O}_4$  with Cu/Mn molar ratio of 1:1 calcined at 400 °C. The  $\text{CuO}_x/\text{Cu}_{1.5}\text{Mn}_{1.5}\text{O}_4$  can completely convert CO to  $\text{CO}_2$  at 75 °C, especially at low temperatures.  $T_{50}$  (the temperature of 50% of CO conversion) is only 41 °C. The  $\text{CO}_2$  yield in the CO oxidation has been shown in Figure S8a, which presents nearly 100% yield. Moreover, they have been compared with previous works (Table S1), which also presents a better catalytic property. Other samples exhibit a relatively lower catalytic activity performance with higher  $T_{100}$  (the temperature of 100% of CO conversion) and  $T_{50}$  (the temperature of 50% of CO conversion) in Figure 3. The 100% CO conversion was accomplished for individual CuO,  $\text{Cu}_2\text{O}$ -CuO, and  $\text{MnO}_x$  samples at 140 °C, 130 °C, and 200 °C, respectively. The individual  $\text{CuO}_x$  and  $\text{MnO}_x$  particles show poorer performance than  $\text{CuO}_x/\text{Cu}_{1.5}\text{Mn}_{1.5}\text{O}_4$ , implying that the synergistic effect between  $\text{CuO}_x$  and  $\text{MnO}_x$  may promote its catalytic activity that is not presented in the individual components. As shown in Figure S8b, the sample of physical mixing of  $\text{CuO}_x + \text{MnO}_x$  was also prepared, which exhibits the poor catalytic performance for CO

oxidation. The stability of the  $\text{CuO}_x/\text{Cu}_{1.5}\text{Mn}_{1.5}\text{O}_4$  was also tested at 60 °C. The negligible decline of activity can be observed during 30 h testing from Figure S9, which implies the excellent stability of  $\text{CuO}_x/\text{Cu}_{1.5}\text{Mn}_{1.5}\text{O}_4$  for CO oxidation reaction.

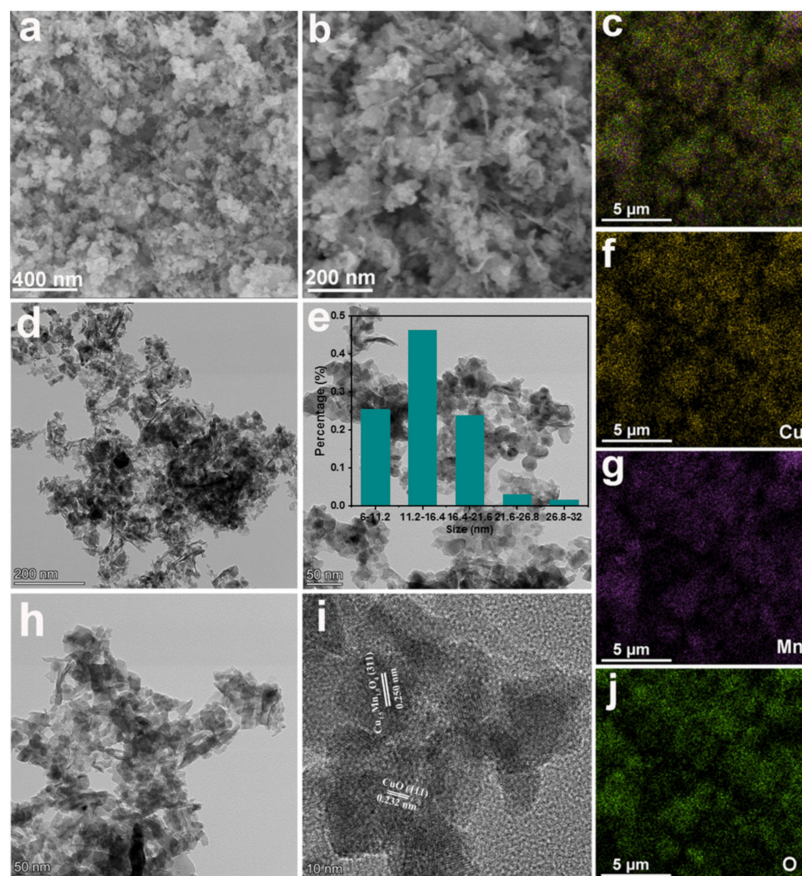


**Figure 2.** (a,b) the SEM images; (d,e,h) TEM images; (i) HRTEM image; and (c,f,g,j) the corresponding element mapping patterns of  $\text{CuO}_x/\text{Cu}_{1.5}\text{Mn}_{1.5}\text{O}_4$ .

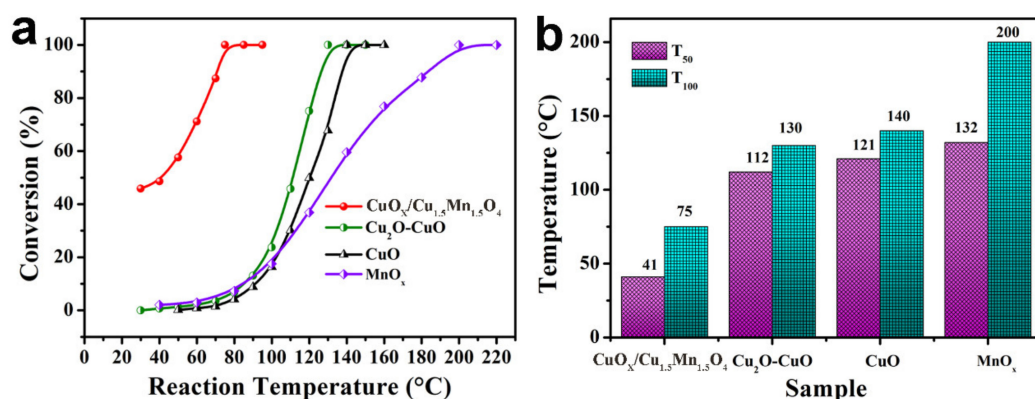


**Figure 3.** (a,b) The CO conversion performances on various catalysts.

The X-ray photoelectron spectra (XPS) were used to investigate the chemical states of samples. The XPS spectrum in Figure 4 and Figure S10 indicate the coexistence of the Cu, Mn, and O elements. Two peaks at about 931.1 and 950.9 eV, respectively, shown in Figure 4a refer to the  $\text{Cu}^+$  or  $\text{Cu}^0$  due to the fact that their binding energies are basically the same [31,54].  $\text{Cu}^0$  is unstable at room temperature and easily oxidized to copper oxide. The  $\text{CuO}_x/\text{Cu}_{1.5}\text{Mn}_{1.5}\text{O}_4$  nanocomposites were acquired after being calcined at high

temperature in air. Therefore, the peak is assigned to  $\text{Cu}^+$  because of the successful synthesis of  $\text{CuO}_x/\text{Cu}_{1.5}\text{Mn}_{1.5}\text{O}_4$  nanocomposites. The two main peaks have small shoulder peaks that appeared at 933.3 and 953.4 eV, relating to the  $\text{Cu}^{2+}$  [55–58]. The XPS analysis results imply that  $\text{Cu}^+$  and  $\text{Cu}^{2+}$  coexist on the surfaces of the  $\text{CuO}_x/\text{Cu}_{1.5}\text{Mn}_{1.5}\text{O}_4$ . As shown in Figure 4b, the asymmetrical Mn 2p spectra of individual  $\text{MnO}_x$  catalysts could be fitted into four components based on their binding energies. The binding energies of 640.2 eV, 641.2 eV, 642.5 eV, and 646.0 eV correspond to  $\text{Mn}^{2+}$ ,  $\text{Mn}^{3+}$ ,  $\text{Mn}^{4+}$  species, and the satellite peak, respectively [59]. The O 1s XPS spectrum of samples can be divided into three single peaks (Figure 4c), corresponding to surface lattice oxygen ( $\text{O}_\alpha$ ), surface adsorbed oxygen ( $\text{O}_\beta$ ), and adsorbed molecular water species ( $\text{O}_\gamma$ ), respectively [14,60–62]. The  $\text{CuO}_x/\text{Cu}_{1.5}\text{Mn}_{1.5}\text{O}_4$  demonstrates the highest surface adsorbed oxygen, which is beneficial to the adsorption of  $\text{O}_2$  molecules, and thus help to improve catalytic performance.

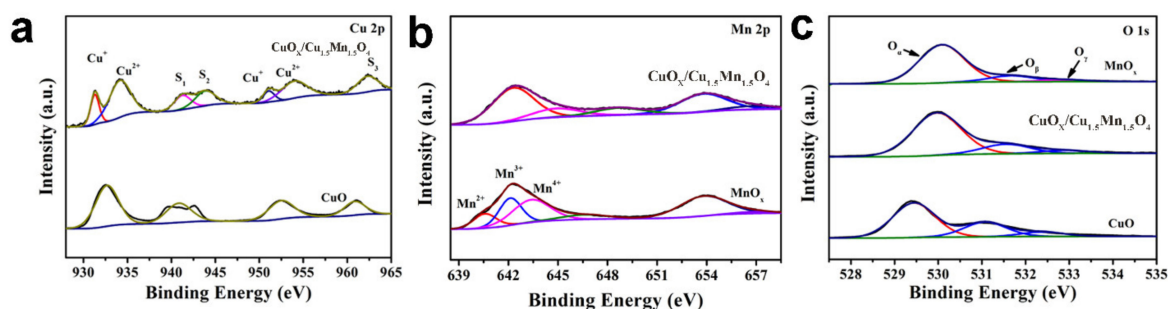


**Figure 4.** (a) Cu 2p; (b) Mn 2p; (c) O 1s spectra of  $\text{MnO}_x$ ,  $\text{CuO}_x/\text{Cu}_{1.5}\text{Mn}_{1.5}\text{O}_4$ , and  $\text{CuO}$  catalysts, respectively.

As shown in Figure 5a, the reduction property of prepared samples was investigated by hydrogen temperature-programmed reduction ( $\text{H}_2$ -TPR). A peak at 200 °C–400 °C was presented for an individual  $\text{CuO}$  sample, attributing to the gradual reduction of copper oxide [30]. In addition, two  $\text{H}_2$  reduction peaks at 245 °C and 364 °C occurred for an  $\text{MnO}_x$  sample, which correspond to the gradual reduction of  $\text{MnO}_2 \rightarrow \text{Mn}_3\text{O}_4 \rightarrow \text{MnO}$  [23,39,59]. For  $\text{CuO}_x/\text{Cu}_{1.5}\text{Mn}_{1.5}\text{O}_4$  nanocomposite, the first peak at below 158 °C refers to the reduction of fine  $\text{CuO}$  to  $\text{Cu}$  or  $\text{MnO}_2$  to  $\text{Mn}_3\text{O}_4$ . Other peaks at 174 °C and 201 °C correspond to the gradual reduction of  $\text{Cu}_{1.5}\text{Mn}_{1.5}\text{O}_4$  oxides [63]. The lower reduction temperature for  $\text{CuO}_x/\text{Cu}_{1.5}\text{Mn}_{1.5}\text{O}_4$  compared with individual  $\text{CuO}_x$  and  $\text{MnO}_x$  indicates the strong synergistic effect between  $\text{CuO}_x$  and  $\text{MnO}_x$ . The strong interactions in  $\text{CuO}_x/\text{Cu}_{1.5}\text{Mn}_{1.5}\text{O}_4$  are often related to the abundant oxygen vacancies, which can promote catalytic performance. The oxygen storage capacity (OSC) of catalysts was assessed by oxygen temperature-programmed desorption ( $\text{O}_2$ -TPD). In Figure 5b, the temperature below 200 °C is due to the desorption of surface oxygen species ( $\text{O}_\beta$ ) [64]. The second peak, appearing at 250–550 °C, corresponds to the overflow of surface lattice oxygen ( $\text{O}_\alpha$ ). The high-temperature zone at above 550 °C is related to the bulk lattice oxygen species [63]. The  $\text{CuO}_x/\text{Cu}_{1.5}\text{Mn}_{1.5}\text{O}_4$  shows the highest amount of adsorbed oxygen species compared with other samples, confirming the higher oxygen capacity that is conducive to the promotion of catalytic performance.

To elucidate the effects of surface  $\text{CuO}_x$  species and the oxygen vacancies in  $\text{CuO}_x/\text{Cu}_{1.5}\text{Mn}_{1.5}\text{O}_4$  in detail, the  $\text{Cu}_{1.5}\text{Mn}_{1.5}\text{O}_4$  was fabricated by changing the types of copper salt in the synthesis process to investigate the structure-activity relationships. The  $\text{Cu}^{2+}$  and  $\text{Mn}^{4+}$  proportion was evaluated by XPS (Figure 6d). It indicates that the ratio of  $\text{Cu}^{2+}$  and  $\text{Mn}^{4+}$  in  $\text{CuO}_x/\text{Cu}_{1.5}\text{Mn}_{1.5}\text{O}_4$  is higher than  $\text{Cu}_{1.5}\text{Mn}_{1.5}\text{O}_4$  sample. The higher contents of  $\text{Cu}^{2+}$  and  $\text{Mn}^{4+}$  are beneficial to the formation of  $\text{Cu}^{2+}-\text{O}^{2-}-\text{Mn}^{4+}$  entities at the two-phase interface [36]. As reported in the studies [63,65], the presence of abundant  $\text{Mn}^{4+}$  proportion can create many adsorbed oxygen species [63]. In addition, the ratios of  $\text{Cu}^+/\text{Cu}^{2+}$  in different samples show a change by altering the types of copper salts in the synthetic process (Table S2). The  $\text{CuO}_x/\text{Cu}_{1.5}\text{Mn}_{1.5}\text{O}_4$  exhibits a higher  $\text{Cu}^{2+}$  ratio than  $\text{Cu}_{1.5}\text{Mn}_{1.5}\text{O}_4$ , which corresponds to XRD results that the  $\text{CuO}_x/\text{Cu}_{1.5}\text{Mn}_{1.5}\text{O}_4$  shows the

higher intensity of the CuO diffraction peaks. The XPS results indicate that the  $\text{Cu}^{2+}$  and  $\text{Mn}^{4+}$  proportion can be engineered by changing the component of Cu-based oxides in the synthetic process.

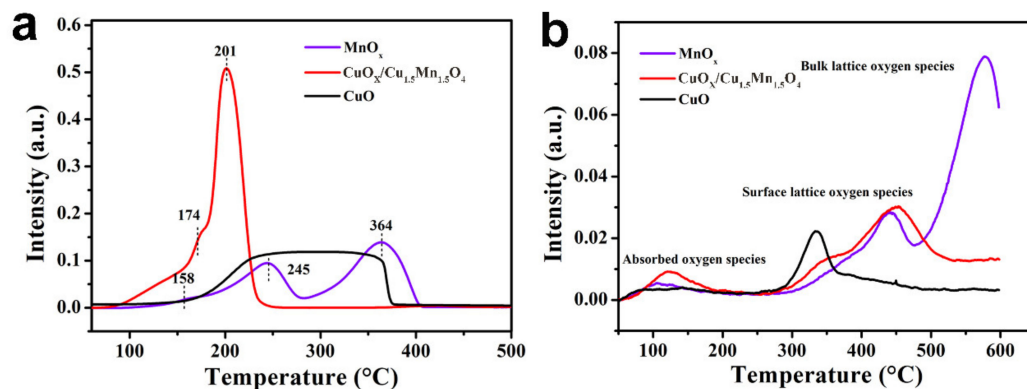


Figure 5. (a)  $\text{H}_2$ -TPR; (b)  $\text{O}_2$ -TPD profiles of  $\text{MnO}_x$ ,  $\text{CuO}_x/\text{Cu}_{1.5}\text{Mn}_{1.5}\text{O}_4$ , and  $\text{CuO}$  catalysts, respectively.

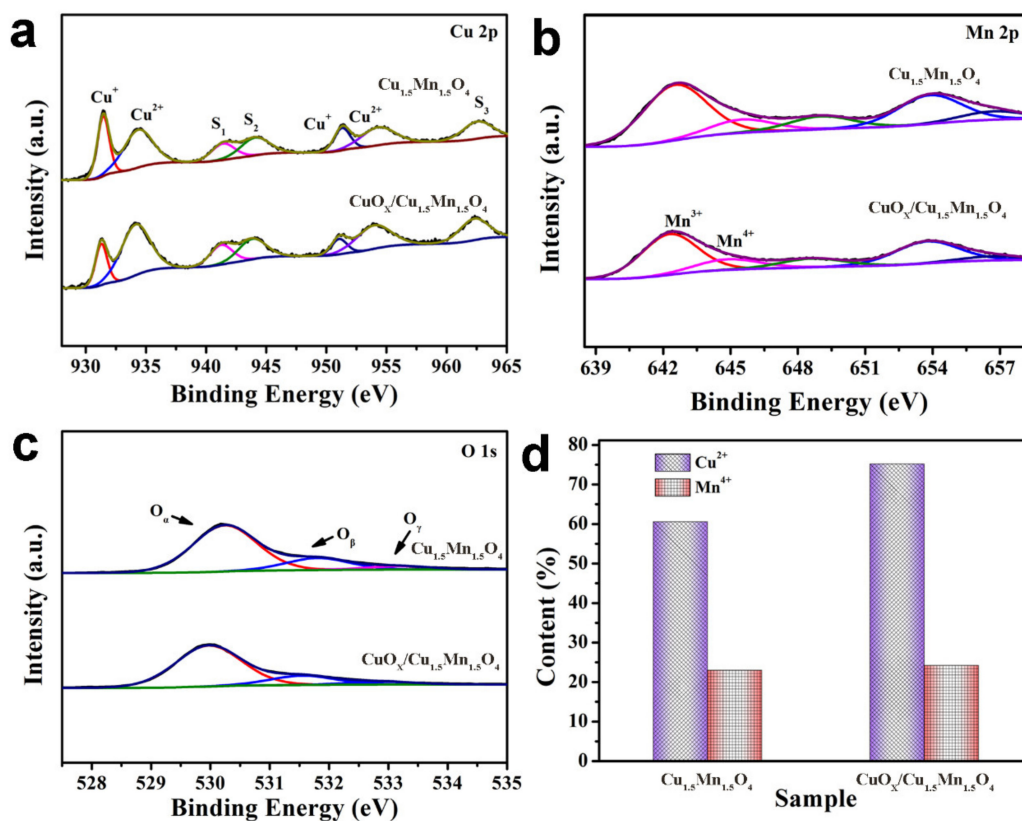
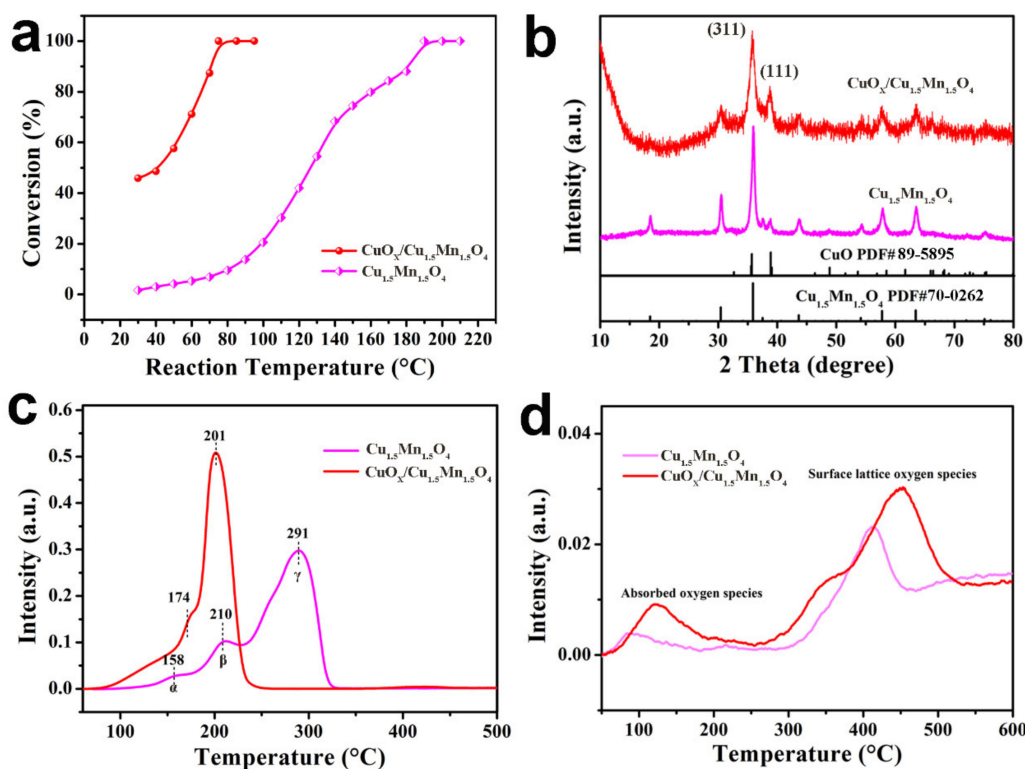


Figure 6. (a) Cu 2p; (b) Mn 2p; (c) O 1s spectra; (d) the contents of  $\text{Cu}^{2+}$  and  $\text{Mn}^{4+}$  in  $\text{Cu}_{1.5}\text{Mn}_{1.5}\text{O}_4$  and  $\text{CuO}_x/\text{Cu}_{1.5}\text{Mn}_{1.5}\text{O}_4$ , respectively.

As shown in Figure 7a, there are obvious differences in catalytic performance after changing the copper salts. The  $\text{Cu}_{1.5}\text{Mn}_{1.5}\text{O}_4$  exhibits poor catalytic activity compared with  $\text{CuO}_x/\text{Cu}_{1.5}\text{Mn}_{1.5}\text{O}_4$  at the same condition. Herein, the performance of catalysts can be meaningfully boosted by altering the surface  $\text{CuO}_x$  species and the oxygen vacancies in  $\text{CuO}_x/\text{Cu}_{1.5}\text{Mn}_{1.5}\text{O}_4$ . As shown in Figure S11a,b, the  $\text{Cu}_{1.5}\text{Mn}_{1.5}\text{O}_4$  exhibited irregular nanoparticles morphology. The Cu and Mn elements are homogeneously dispersed on the surface of  $\text{Cu}_{1.5}\text{Mn}_{1.5}\text{O}_4$ , and their molar ratio is close to 1.0 (Figure S2), which has no significant difference with  $\text{CuO}_x/\text{Cu}_{1.5}\text{Mn}_{1.5}\text{O}_4$ . The XRD diffraction patterns indicate the

formation of  $\text{Cu}_{1.5}\text{Mn}_{1.5}\text{O}_4$  containing some  $\text{CuO}_x$  (Figure 7b), while the catalytic performance showed obvious differences. The  $\text{CuO}_x/\text{Cu}_{1.5}\text{Mn}_{1.5}\text{O}_4$  exhibits the higher intensity of the CuO diffraction peaks than  $\text{Cu}_{1.5}\text{Mn}_{1.5}\text{O}_4$ . In our previous work [31], the individual  $\text{Cu}_2\text{O}/\text{CuO}$  nanocomposites and CuO can be fabricated by tuning the types of copper salt in the synthesis. The  $\text{Cu}_{1.5}\text{Mn}_{1.5}\text{O}_4$  with different surface  $\text{CuO}_x$  types were fabricated by altering the types of copper salts (+1, +2 valence state) in the synthetic process. Therefore, the different surface types in  $\text{Cu}_{1.5}\text{Mn}_{1.5}\text{O}_4$  depend on the types of copper salts (+1, +2 valence state) in the synthetic process used. The higher content of CuO in  $\text{CuO}_x/\text{Cu}_{1.5}\text{Mn}_{1.5}\text{O}_4$  can significantly enhance redox reaction between Cu and Mn species, promoting charge transfer in nanocomposites, and thus achieving a stronger interaction. From Figure 7c, the  $\text{CuO}_x/\text{Cu}_{1.5}\text{Mn}_{1.5}\text{O}_4$  shows a lower reduction temperature than  $\text{Cu}_{1.5}\text{Mn}_{1.5}\text{O}_4$ , implying the better reducibility. The peak areas for different samples were estimated from the  $\text{H}_2$ -TPR results. In Table S3, the higher peak areas of first peak  $\alpha$  is presented for  $\text{CuO}_x/\text{Cu}_{1.5}\text{Mn}_{1.5}\text{O}_4$ , indicating the ratio of  $\text{Cu}^{2+}$  and  $\text{Mn}^{4+}$  in  $\text{CuO}_x/\text{Cu}_{1.5}\text{Mn}_{1.5}\text{O}_4$ , which is consistent with XPS results. Therefore, we can confirm that CO oxidation activity is heavily dependent on the surface  $\text{CuO}_x$  species in  $\text{CuO}_x/\text{Cu}_{1.5}\text{Mn}_{1.5}\text{O}_4$ . In addition, as shown in Figure 7d, the amounts of oxygen desorption ( $\text{O}_\beta$ ) over the obtained  $\text{CuO}_x/\text{Cu}_{1.5}\text{Mn}_{1.5}\text{O}_4$  are greatly changed by adjusting the surface  $\text{CuO}_x$  species. The  $\text{CuO}_x/\text{Cu}_{1.5}\text{Mn}_{1.5}\text{O}_4$  shows the highest amount of adsorbed oxygen species compared with  $\text{Cu}_{1.5}\text{Mn}_{1.5}\text{O}_4$ , confirming the higher oxygen capacity that is conducive to the promotion of catalytic performance. The  $\text{H}_2$ -TPR analysis results indicate that the interaction of nanocomposites could be manipulated by changing the surface compositions of  $\text{CuO}_x/\text{Cu}_{1.5}\text{Mn}_{1.5}\text{O}_4$ . The  $\text{O}_2$ -TPD results further identify the presence of abundant surface-adsorbed oxygen on the surface of  $\text{CuO}_x/\text{Cu}_{1.5}\text{Mn}_{1.5}\text{O}_4$ . Therefore, the construction of  $\text{CuO}_x/\text{Cu}_{1.5}\text{Mn}_{1.5}\text{O}_4$  with abundant surface  $\text{CuO}_x$  species not only strengthens the interactions in  $\text{CuO}_x/\text{Cu}_{1.5}\text{Mn}_{1.5}\text{O}_4$ , but also facilitates the absorption and activation of surface oxygen species.



**Figure 7.** (a) The CO conversion performances; (b) the powder XRD patterns; (c)  $\text{H}_2$ -TPR; (d)  $\text{O}_2$ -TPD profiles of  $\text{Cu}_{1.5}\text{Mn}_{1.5}\text{O}_4$  and  $\text{CuO}_x/\text{Cu}_{1.5}\text{Mn}_{1.5}\text{O}_4$ , respectively.

Density functional theory (DFT) calculations were implemented to understand the intrinsic reason about the mechanism of CO and O<sub>2</sub> adsorption and the subsequent oxidation process for CuO<sub>x</sub>/Cu<sub>1.5</sub>Mn<sub>1.5</sub>O<sub>4</sub>. The adsorption configurations of CO and O<sub>2</sub> molecules on the CuO, Cu<sub>1.5</sub>Mn<sub>1.5</sub>O<sub>4</sub>, and CuO<sub>x</sub>/Cu<sub>1.5</sub>Mn<sub>1.5</sub>O<sub>4</sub> are shown in Figure 8. It is found that CO is adsorbed on the surface of CuO and Cu<sub>1.5</sub>Mn<sub>1.5</sub>O<sub>4</sub> with the adsorption energy of  $-0.316$  eV and  $-0.164$  eV, respectively. The adsorption energy of CO molecules adsorbed at the CuO<sub>x</sub>/Cu<sub>1.5</sub>Mn<sub>1.5</sub>O<sub>4</sub> surface is  $-1.346$  eV, which are lower than that on CuO and Cu<sub>1.5</sub>Mn<sub>1.5</sub>O<sub>4</sub>. In addition, the adsorption energy of O<sub>2</sub> molecules on CuO<sub>x</sub>/Cu<sub>1.5</sub>Mn<sub>1.5</sub>O<sub>4</sub> surface is  $-1.018$  eV, which is much lower than the  $0.026$  eV and  $-0.962$  eV for CuO and Cu<sub>1.5</sub>Mn<sub>1.5</sub>O<sub>4</sub>. The lower adsorption energy indicates that gas molecules are easier to adsorb on the surface of CuO<sub>x</sub>/Cu<sub>1.5</sub>Mn<sub>1.5</sub>O<sub>4</sub>. In summary, DFT calculation showed that construction of CuO<sub>x</sub>/Cu<sub>1.5</sub>Mn<sub>1.5</sub>O<sub>4</sub> nanocomposite with abundant surface CuO<sub>x</sub> species and oxygen vacancies significantly improved the adsorption capacity of CO and O<sub>2</sub> molecules, and thus is more beneficial for CO oxidation activity.

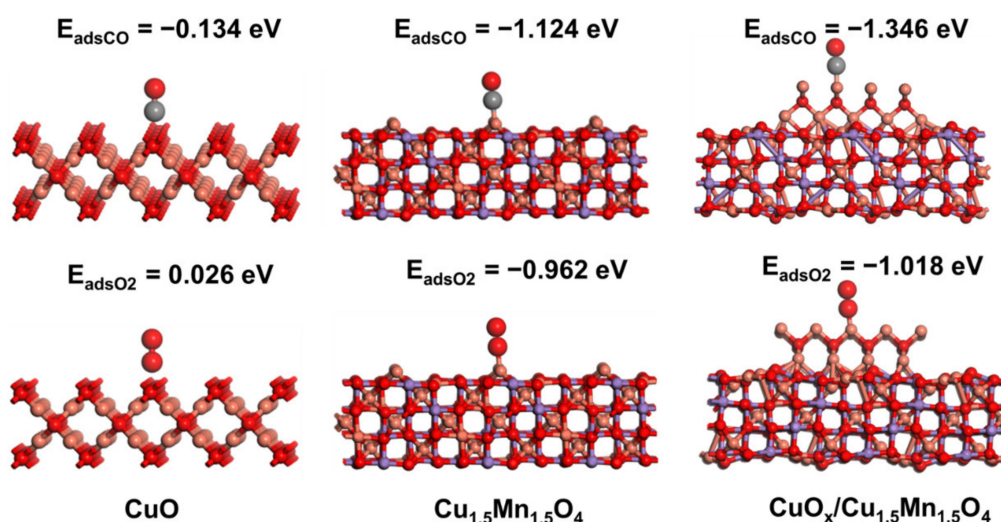


**Figure 8.** The side views of CO and O<sub>2</sub> adsorption on the surfaces of CuO, Cu<sub>1.5</sub>Mn<sub>1.5</sub>O<sub>4</sub>, and CuO<sub>x</sub>/Cu<sub>1.5</sub>Mn<sub>1.5</sub>O<sub>4</sub>, respectively.

The effects of surface CuO<sub>x</sub> species and the oxygen vacancies in composite oxide can be clarified based on the above results. In Figure 9, the catalytic property of the CuO<sub>x</sub>/Cu<sub>1.5</sub>Mn<sub>1.5</sub>O<sub>4</sub> is improved compared to Cu<sub>1.5</sub>Mn<sub>1.5</sub>O<sub>4</sub>, which confirms the important role of surface CuO<sub>x</sub> species and oxygen vacancies. After construction of CuO<sub>x</sub>/Cu<sub>1.5</sub>Mn<sub>1.5</sub>O<sub>4</sub> nanocomposite with abundant surface CuO<sub>x</sub> species and oxygen vacancies, the abundant Cu<sup>2+</sup> and Mn<sup>4+</sup> proportions in CuO<sub>x</sub>/Cu<sub>1.5</sub>Mn<sub>1.5</sub>O<sub>4</sub> are higher than in Cu<sub>1.5</sub>Mn<sub>1.5</sub>O<sub>4</sub>, which facilitated the formation of more (Cu<sup>2+</sup>-O<sup>2-</sup>-Mn<sup>4+</sup>) entities at the two interfaces. In addition, the construction of CuO<sub>x</sub>/Cu<sub>1.5</sub>Mn<sub>1.5</sub>O<sub>4</sub> nanocomposites is beneficial for enhancing the synergetic interaction between MnO<sub>x</sub> species and CuO<sub>x</sub> species, which promotes the massive production of surface adsorbed oxygen species [36]. In CO oxidation, surface CuO<sub>x</sub> species and oxygen vacancies play significant roles in catalytic activity. The abundant surface CuO<sub>x</sub> species and oxygen vacancies could preferentially adsorb CO and O<sub>2</sub> molecules [22], and the adsorbed O<sub>2</sub> reacts with CO to form CO<sub>2</sub>, which ultimately enhances catalytic activity.

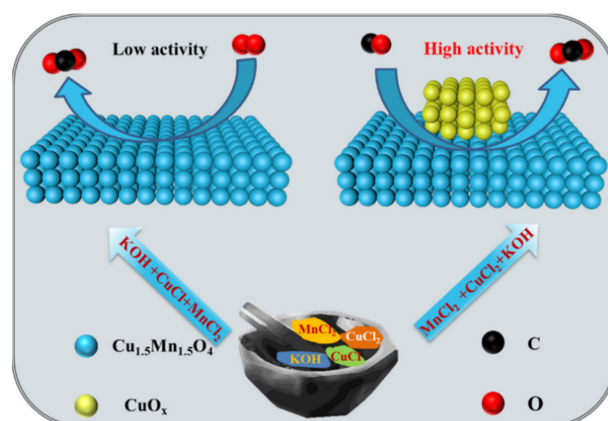


**Figure 9.** Reaction mechanisms of  $\text{CuO}_x/\text{Cu}_{1.5}\text{Mn}_{1.5}\text{O}_4$  toward CO oxidation.

### 3. Materials and Methods

#### 3.1. Materials

Copper (II) chloride ( $\text{CuCl}_2$ , AR), cuprous (I) chloride ( $\text{CuCl}$ , AR), manganese (II) chloride ( $\text{MnCl}_2$ , AR), and potassium hydroxide ( $\text{KOH}$ , AR) were purchased from Tianjin Zhiyuan Chemical Reagents Co., Ltd. (Tianjin, China), which were used without further refinement.

#### 3.2. The Preparation of $\text{CuO}_x/\text{Cu}_{1.5}\text{Mn}_{1.5}\text{O}_4$ Nanocomposite with Various Surface $\text{CuO}_x$ Species and the Oxygen Vacancies

As shown in Scheme 1, in a typical procedure, 1.70 g of  $\text{CuCl}_2$  (10 mmol) and 1.25 g of  $\text{MnCl}_2$  (10 mmol) were mixed well in an agate mortar by grinding. Then 4.49 g of  $\text{KOH}$  (60 mmol) was added into the agate mortar. After continuous grinding for about 1 h, the resulting solid products were sufficiently washed with deionized water and anhydrous ethanol to clear the residual Cl or K species, and then dried at ambient temperature overnight. The final  $\text{CuO}_x/\text{Cu}_{1.5}\text{Mn}_{1.5}\text{O}_4$  nanocomposites were acquired after calcining the mixtures in the air at  $400\text{ }^\circ\text{C}$  for 2 h ( $5\text{ }^\circ\text{C}/\text{min}$ ). In addition, the  $\text{CuO}_x/\text{Cu}_{1.5}\text{Mn}_{1.5}\text{O}_4$  with different Cu/Mn mole ratios (Cu/Mn = 1:2 and 2:1) were calcined at  $300\text{ }^\circ\text{C}$  or  $500\text{ }^\circ\text{C}$ .

The  $\text{Cu}_{1.5}\text{Mn}_{1.5}\text{O}_4$  nanocomposite (containing some  $\text{CuO}$ ) was also obtained, and only the  $\text{CuCl}_2$  was replaced by  $\text{CuCl}$  during the solvent-free synthesis route.

#### 3.3. The Preparation of $\text{MnO}_x$

As a comparison, the individual  $\text{MnO}_x$  particles were also fabricated by straightforward grinding  $\text{MnCl}_2$  with  $\text{KOH}$  under a similar process.

#### 3.4. The Preparation of $\text{Cu}_2\text{O}/\text{CuO}$ and $\text{CuO}$

The  $\text{Cu}_2\text{O}/\text{CuO}$  nanocomposite was fabricated according to our previous work [31]. The 0.99 g of  $\text{CuCl}$  (10 mmol) and 1.68 g of  $\text{KOH}$  (30 mmol) were ground in the agate mortar for 1 h. The other parameters are consistent with the  $\text{CuO}_x/\text{Cu}_{1.5}\text{Mn}_{1.5}\text{O}_4$  nanocomposite above.

In addition, the  $\text{CuO}$  was also prepared by mixing  $\text{CuCl}_2$  and  $\text{KOH}$  in the agate mortar. The sample of physical mixing of  $\text{CuO}_x + \text{MnO}_x$  was also prepared by straightforward grinding  $\text{CuO}$  and  $\text{MnO}_x$ , and then calcining the mixtures in the air at  $400\text{ }^\circ\text{C}$  for 2 h ( $5\text{ }^\circ\text{C}/\text{min}$ ).

#### 3.5. The Characterization and Testing Processes of Catalyst

XRD, SEM, HRTEM, EDS, XPS,  $\text{H}_2$ -TPR, and  $\text{O}_2$ -TPD were implemented to investigate the morphology and structure of  $\text{CuO}_x/\text{Cu}_{1.5}\text{Mn}_{1.5}\text{O}_4$  nanocomposites. Detailed characterization and testing processes are presented in the Supplementary Materials.

#### 4. Conclusions

In summary, the  $\text{Cu}_{1.5}\text{Mn}_{1.5}\text{O}_4$  with different surface  $\text{CuO}_x$  types were fabricated by altering the types of copper salts (+1, +2 valence state) in the synthetic process. The higher content of CuO in  $\text{CuO}_x/\text{Cu}_{1.5}\text{Mn}_{1.5}\text{O}_4$  can significantly enhance redox reaction between Cu and Mn species, promoting charge transfer in nanocomposites, thus achieving a stronger interaction. In addition, the higher ratio of  $\text{Cu}^{2+}$  and  $\text{Mn}^{4+}$  is beneficial to the formation of  $\text{Cu}^{2+}-\text{O}^{2-}-\text{Mn}^{4+}$  entities at the two-phase interface, which produced abundant surface  $\text{CuO}_x$  species and oxygen vacancies. DFT calculations suggest that CO and  $\text{O}_2$  molecules are adsorbed on the  $\text{CuO}_x/\text{Cu}_{1.5}\text{Mn}_{1.5}\text{O}_4$  surface with relatively optimal adsorption energy, resulting in the highest CO oxidation activity. The as-synthesized  $\text{CuO}_x/\text{Cu}_{1.5}\text{Mn}_{1.5}\text{O}_4$  delivers excellent CO catalytic performance compared with individual  $\text{CuO}_x$  and  $\text{MnO}_x$  particles. The CO is completely converted to  $\text{CO}_2$  at 75 °C when  $\text{CuO}_x/\text{Cu}_{1.5}\text{Mn}_{1.5}\text{O}_4$  is involved. This work opens new avenues for the efficient and sustainable production of heterogeneous metal oxides with an outstanding catalytic performance.

**Supplementary Materials:** The following supporting information can be downloaded at: <https://www.mdpi.com/article/10.3390/ijms23126856/s1>. References [66–68] are cited in Supplementary Materials.

**Author Contributions:** Conceptualization, B.L. and Y.L.; methodology, B.L.; software, H.W.; validation, B.L., Y.L. and S.L.; formal analysis, B.L.; investigation, B.L.; resources, Y.L. and Y.C.; data curation, M.X.; writing—original draft preparation, B.L.; writing—review and editing, B.L. and Y.L.; visualization, B.L.; supervision, Y.L. and Y.C.; project administration, Y.L. and Y.C.; funding acquisition, Y.L. and Y.C. All authors have read and agreed to the published version of the manuscript.

**Funding:** This work was financially supported by the National Natural Science Foundation of China (Nos. 21766036 and 52100166), the Natural Science Foundation of Xinjiang Province (No. 2019D04005), the Graduate Innovation Project of Xinjiang Province (No. XJ2021G037), and the Key Research and Development Project of Xinjiang Province (No. 2020B02008).

**Institutional Review Board Statement:** This study did not require ethical approval.

**Informed Consent Statement:** This study did not involve humans.

**Data Availability Statement:** The study did not report any data, we choose to exclude this statement.

**Conflicts of Interest:** The authors declare no conflict of interest.

#### References

1. Hu, Z.; Liu, X.; Meng, D.; Guo, Y.; Guo, Y.; Lu, G. Effect of Ceria ceria crystal plane on the physicochemical and catalytic properties of Pd/Ceria for CO and propane oxidation. *ACS Catal.* **2016**, *6*, 2265–2279. [CrossRef]
2. Du, P.-P.; Hu, X.-C.; Wang, X.; Ma, C.; Du, M.; Zeng, J.; Jia, C.-J.; Huang, Y.-Y.; Si, R. Synthesis and metal-support interaction of subnanometer copper-palladium bimetallic oxide clusters for catalytic oxidation of carbon monoxide. *Inorg. Chem. Front.* **2017**, *4*, 668–674. [CrossRef]
3. Guo, X.; Li, J.; Zhou, R. Catalytic performance of manganese doped  $\text{CuO}-\text{CeO}_2$  catalysts for selective oxidation of CO in hydrogen-rich gas. *Fuel* **2016**, *163*, 56–64. [CrossRef]
4. Zou, W.X.; Liu, L.C.; Zhang, L.; Li, L.; Cao, Y.; Wang, X.B.; Tang, C.J.; Gao, F.; Dong, L. Crystal-plane effects on surface and catalytic properties of  $\text{Cu}_2\text{O}$  nanocrystals for NO reduction by CO. *Appl. Catal. A Gen.* **2015**, *505*, 334–343. [CrossRef]
5. Tao, L.; Shi, Y.; Huang, Y.-C.; Chen, R.; Zhang, Y.; Huo, J.; Zou, Y.; Yu, G.; Luo, J.; Dong, C.-L.; et al. Interface engineering of Pt and  $\text{CeO}_2$  nanorods with unique interaction for methanol oxidation. *Nano Energy* **2018**, *53*, 604–612. [CrossRef]
6. Sun, L.; Zhan, W.W.; Li, Y.A.; Wang, F.; Zhang, X.L.; Han, X.G. Understanding the facet-dependent catalytic performance of hematite microcrystals in a CO oxidation reaction. *Inorg. Chem. Front.* **2018**, *5*, 2332–2339. [CrossRef]
7. Singhanian, N.; Anumol, E.A.; Ravishankar, N.; Madras, G. Influence of  $\text{CeO}_2$  morphology on the catalytic activity of  $\text{CeO}_2$ -Pt hybrids for CO oxidation. *Dalton Trans.* **2013**, *42*, 15343–15354. [CrossRef]
8. Yang, J.; Hu, S.; Fang, Y.; Hoang, S.; Li, L.; Yang, W.; Liang, Z.; Wu, J.; Hu, J.; Xiao, W.; et al. Oxygen Vacancy promoted  $\text{O}_2$  activation over perovskite oxide for low-temperature CO oxidation. *ACS Catal.* **2019**, *9*, 9751–9763. [CrossRef]
9. Lykaki, M.; Pachatouridou, E.; Carabineiro, S.A.; Iliopoulou, E.; Andriopoulou, C.; Kallithrakas-Kontos, N.; Boghosian, S.; Konsolakis, M. Ceria nanoparticles shape effects on the structural defects and surface chemistry: Implications in CO oxidation by Cu/ $\text{CeO}_2$  catalysts. *Appl. Catal. B Environ.* **2018**, *230*, 18–28. [CrossRef]
10. Lawrence, N.J.; Brewer, J.R.; Wang, L.; Wu, T.-S.; Wells-Kingsbury, J.; Ihrig, M.M.; Wang, G.; Soo, Y.-L.; Mei, W.-N.; Cheung, C.L. Defect engineering in cubic cerium oxide nanostructures for catalytic oxidation. *Nano Lett.* **2011**, *11*, 2666–2671. [CrossRef]

11. Li, W.; Feng, X.L.; Zhang, Z.; Jin, X.; Liu, D.P.; Zhang, Y. A controllable surface etching strategy for well-defined spiny yolk@shell CuO@CeO<sub>2</sub> cubes and their catalytic performance boost. *Adv. Funct. Mater.* **2018**, *28*, 1802559. [[CrossRef](#)]
12. Ma, B.; Kong, C.; Lv, J.; Zhang, X.; Yang, S.; Yang, T.; Yang, Z. Cu–Cu<sub>2</sub>O heterogeneous architecture for the enhanced CO catalytic oxidation. *Adv. Mater. Interfaces* **2020**, *7*, 1901643. [[CrossRef](#)]
13. Liu, B.L.; Li, Y.Z.; Qing, S.J.; Wang, K.; Xie, J.; Cao, Y.L. Engineering CuO<sub>x</sub>–ZrO<sub>2</sub>–CeO<sub>2</sub> nanocatalysts with abundant surface Cu species and oxygen vacancies toward high catalytic performance in CO oxidation and 4-nitrophenol reduction. *CrystEngComm* **2020**, *22*, 4005–4013. [[CrossRef](#)]
14. Fang, Y.; Chi, X.; Li, L.; Yang, J.; Liu, S.; Lu, X.; Xiao, W.; Wang, L.; Luo, Z.; Yang, W.; et al. Elucidating the nature of the Cu(I) active site in CuO/TiO<sub>2</sub> for excellent low-temperature CO oxidation. *ACS Appl. Mater. Interfaces* **2020**, *12*, 7091–7101. [[CrossRef](#)]
15. Jin, X.; Duan, Y.; Liu, D.P.; Feng, X.L.; Li, W.; Zhang, Z.; Zhang, Y. CO oxidation catalyzed by two-dimensional Co<sub>3</sub>O<sub>4</sub>/CeO<sub>2</sub> nanosheets. *ACS Appl. Nano Mater.* **2019**, *2*, 5769–5778. [[CrossRef](#)]
16. Wang, H.; Mao, D.; Qi, J.; Zhang, Q.H.; Ma, X.H.; Song, S.Y.; Gu, L.; Yu, R.B.; Wang, D. Hollow multishelled structure of heterogeneous Co<sub>3</sub>O<sub>4</sub>–CeO<sub>2</sub>–*x* nanocomposite for CO catalytic oxidation. *Adv. Funct. Mater.* **2019**, *29*, 1806588. [[CrossRef](#)]
17. Yuan, C.; Wang, H.-G.; Liu, J.; Wu, Q.; Duan, Q.; Li, Y. Facile synthesis of Co<sub>3</sub>O<sub>4</sub>–CeO<sub>2</sub> composite oxide nanotubes and their multifunctional applications for lithium ion batteries and CO oxidation. *J. Colloid Interface Sci.* **2017**, *494*, 274–281. [[CrossRef](#)]
18. Chen, K.; Ling, J.L.; Wu, C.D. In situ generation and stabilization of accessible Cu/Cu<sub>2</sub>O hetero-junctions inside organic frameworks for highly efficient catalysis. *Angew. Chem. Int. Ed. Engl.* **2020**, *59*, 1925–1931. [[CrossRef](#)]
19. Liu, A.; Liu, L.; Cao, Y.; Wang, J.; Si, R.; Gao, F.; Dong, L. Controlling dynamic structural transformation of atomically dispersed CuO<sub>x</sub> species and influence on their catalytic performances. *ACS Catal.* **2019**, *9*, 9840–9851. [[CrossRef](#)]
20. Jampaiah, D.; Velisoju, V.K.; Devaiah, D.; Singh, M.; Mayes, E.L.H.; Coyle, V.E.; Reddy, B.M.; Bansal, V.; Bhargava, S.K. Flower-like Mn<sub>3</sub>O<sub>4</sub>/CeO<sub>2</sub> microspheres as an efficient catalyst for diesel soot and CO oxidation: Synergistic effects for enhanced catalytic performance. *Appl. Surf. Sci.* **2019**, *473*, 209–221. [[CrossRef](#)]
21. Peng, H.; Rao, C.; Zhang, N.; Wang, X.; Liu, W.; Mao, W.; Han, L.; Zhang, P.; Dai, S. Confined ultrathin Pd–Ce nanowires with outstanding moisture and SO<sub>2</sub> tolerance in methane combustion. *Angew. Chem. Int. Ed.* **2018**, *57*, 8953–8957. [[CrossRef](#)]
22. Liu, B.L.; Li, Y.Z.; Cao, Y.L.; Wang, L.; Qing, S.J.; Wang, K.; Jia, D.Z. Optimum balance of Cu<sup>+</sup> and oxygen vacancies of CuO<sub>x</sub>–CeO<sub>2</sub> composites for CO oxidation based on thermal treatment. *Eur. J. Inorg. Chem.* **2019**, *2019*, 1714–1723. [[CrossRef](#)]
23. Bai, B.Y.; Li, J.H.; Hao, J.M. 1D–MnO<sub>2</sub>, 2D–MnO<sub>2</sub> and 3D–MnO<sub>2</sub> for low-temperature oxidation of ethanol. *Appl. Catal. B Environ.* **2015**, *164*, 241–250. [[CrossRef](#)]
24. Wang, M.; Liu, H.; Huang, Z.-H.; Kang, F. Activated carbon fibers loaded with MnO<sub>2</sub> for removing NO at room temperature. *Chem. Eng. J.* **2014**, *256*, 101–106. [[CrossRef](#)]
25. Chen, H.; Wang, Y.; Lv, Y.-K. Catalytic oxidation of NO over MnO<sub>2</sub> with different crystal structures. *RSC Adv.* **2016**, *6*, 54032–54040. [[CrossRef](#)]
26. Wang, K.; Cao, Y.L.; Hu, J.D.; Li, Y.Z.; Xie, J.; Jia, D.Z. Solvent-free chemical approach to synthesize various morphological Co<sub>3</sub>O<sub>4</sub> for CO oxidation. *ACS Appl. Mater. Interfaces* **2017**, *9*, 16128–16137. [[CrossRef](#)] [[PubMed](#)]
27. Wang, K.; Liu, B.L.; Cao, Y.L.; Li, Y.Z.; Jia, D.Z. V-modified Co<sub>3</sub>O<sub>4</sub> nanorods with superior catalytic activity and thermostability for CO oxidation. *CrystEngComm* **2018**, *20*, 5191–5199. [[CrossRef](#)]
28. Zhang, C.; Zhang, L.; Xu, G.C.; Ma, X.; Xu, J.L.; Zhang, L.; Qi, C.L.; Xie, Y.Y.; Sun, Z.P.; Jia, D.Z. Hollow and core–shell nanostructure Co<sub>3</sub>O<sub>4</sub> derived from a metal formate framework toward high catalytic activity of CO oxidation. *ACS Appl. Nano Mater.* **2018**, *1*, 800–806. [[CrossRef](#)]
29. Zhang, R.R.; Hu, L.; Bao, S.X.; Li, R.; Gao, L.; Li, R.; Chen, Q.W. Surface polarization enhancement: High catalytic performance of Cu/CuO<sub>x</sub>/C nanocomposites derived from Cu–BTC for CO oxidation. *J. Mater. Chem. A* **2016**, *4*, 8412–8420. [[CrossRef](#)]
30. Wei, B.; Yang, N.T.; Pang, F.; Ge, J.P. Cu<sub>2</sub>O–CuO hollow nanospheres as a heterogeneous catalyst for synergetic oxidation of CO. *J. Phys. Chem. C* **2018**, *122*, 19524–19531. [[CrossRef](#)]
31. Liu, B.L.; Li, Y.Z.; Wang, K.; Cao, Y.L. The solid-state in situ construction of Cu<sub>2</sub>O/CuO hetero-structures with adjustable phase compositions to promote CO oxidation activity. *CrystEngComm* **2020**, *22*, 7808–7815. [[CrossRef](#)]
32. Li, Y.; Shen, W. Morphology-dependent nanocatalysts: Rod-shaped oxides. *Chem. Soc. Rev.* **2014**, *43*, 1543–1574. [[CrossRef](#)]
33. Zhang, J.; Cao, Y.; Wang, C.-A.; Ran, R. Design and preparation of MnO<sub>2</sub>/CeO<sub>2</sub>–MnO<sub>2</sub> double-shelled binary oxide hollow spheres and their application in CO oxidation. *ACS Appl. Mater. Interfaces* **2016**, *8*, 8670–8677. [[CrossRef](#)]
34. Elias, J.S.; Artrith, N.; Bugnet, M.; Giordano, L.; Botton, G.A.; Kolpak, A.M.; Shao-Horn, Y. Elucidating the nature of the active phase in copper/ceria catalysts for CO oxidation. *ACS Catal.* **2016**, *6*, 1675–1679. [[CrossRef](#)]
35. He, J.; Chen, D.; Li, N.; Xu, Q.; Li, H.; He, J.; Lu, J. Hollow mesoporous Co<sub>3</sub>O<sub>4</sub>–CeO<sub>2</sub> composite nanotubes with open ends for efficient catalytic CO oxidation. *ChemSusChem* **2019**, *12*, 1084–1090. [[CrossRef](#)]
36. Wang, Y.; Yang, D.; Li, S.; Zhang, L.; Zheng, G.; Guo, L. Layered copper manganese oxide for the efficient catalytic CO and VOCs oxidation. *Chem. Eng. J.* **2018**, *357*, 258–268. [[CrossRef](#)]
37. Zeng, S.H.; Wang, Y.; Ding, S.P.; Sattler, J.J.H.B.; Borodina, E.; Zhang, L.; Weckhuysen, B.M.; Su, H.Q. Active sites over CuO/CeO<sub>2</sub> and inverse CeO<sub>2</sub>/CuO catalysts for preferential CO oxidation. *J. Power Sources* **2014**, *256*, 301–311. [[CrossRef](#)]
38. Chen, A.; Yu, X.; Zhou, Y.; Miao, S.; Li, Y.; Kuld, S.; Sehested, J.; Liu, J.; Aoki, T.; Hong, S.; et al. Structure of the catalytically active copper–ceria interfacial perimeter. *Nat. Catal.* **2019**, *2*, 334–341. [[CrossRef](#)]

39. Chen, G.; Song, G.; Zhao, W.; Gao, D.; Wei, Y.; Li, C. Carbon sphere-assisted solution combustion synthesis of porous/hollow structured CeO<sub>2</sub>-MnO<sub>x</sub> catalysts. *Chem. Eng. J.* **2018**, *352*, 64–70. [[CrossRef](#)]
40. Pahalagedara, L.; Kriz, D.A.; Wasalathanthri, N.; Weerakkody, C.; Meng, Y.; Dissanayake, S.; Pahalagedara, M.; Luo, Z.; Suib, S.L.; Nandi, P.; et al. Benchmarking of manganese oxide materials with CO oxidation as catalysts for low temperature selective oxidation. *Appl. Catal. B Environ.* **2017**, *204*, 411–420. [[CrossRef](#)]
41. Chen, G.Z.; Xu, Q.H.; Yang, Y.; Li, C.C.; Huang, T.Z.; Sun, G.X.; Zhang, S.X.; Ma, D.L.; Li, X. Facile and mild strategy to construct mesoporous CeO<sub>2</sub>-CuO nanorods with enhanced catalytic activity toward CO oxidation. *ACS Appl. Mater. Interfaces* **2015**, *7*, 23538–23544. [[CrossRef](#)]
42. May, Y.A.; Wei, S.; Yu, W.-Z.; Wang, W.-W.; Jia, C.-J. Highly efficient CuO/ $\alpha$ -MnO<sub>2</sub> catalyst for low-temperature CO oxidation. *Langmuir* **2020**, *36*, 11196–11206. [[CrossRef](#)]
43. Hasegawa, Y.-I.; Maki, R.-U.; Sano, M.; Miyake, T. Preferential oxidation of CO on cop-per-containing manganese oxides. *Appl. Catal. A Gen.* **2009**, *371*, 67–72. [[CrossRef](#)]
44. Elmhamdi, A.; Pascual, L.; Nahdi, K.; Martínez-Arias, A. Structure/redox/activity relationships in CeO<sub>2</sub>/CuMn<sub>2</sub>O<sub>4</sub> CO-PROX catalysts. *Appl. Catal. B Environ.* **2017**, *217*, 1–11. [[CrossRef](#)]
45. Wang, W.-W.; Yu, W.-Z.; Du, P.-P.; Xu, H.; Jin, Z.; Si, R.; Ma, C.; Shi, S.; Jia, C.-J.; Yan, C.-H. Crystal plane effect of ceria on supported copper oxide cluster catalyst for CO oxidation: Importance of metal-support interaction. *ACS Catal.* **2017**, *7*, 1313–1329. [[CrossRef](#)]
46. Liu, Z.Q.; Li, J.H.; Wang, R.G. CeO<sub>2</sub> nanorods supported M-Co bimetallic oxides (M = Fe, Ni, Cu) for catalytic CO and C<sub>3</sub>H<sub>8</sub> oxidation. *J. Colloid Interface Sci.* **2020**, *560*, 91–102. [[CrossRef](#)] [[PubMed](#)]
47. Diao, J.X.; Qiu, Y.; Liu, S.Q.; Wang, W.; Chen, K.; Li, H.L.; Yuan, W.; Qu, Y.T.; Guo, X.H. Inter-facial engineering of W<sub>2</sub>N/WC heterostructures derived from solid-state synthesis: A highly efficient trifunctional electrocatalyst for ORR, OER, and HER. *Adv. Mater.* **2019**, *32*, 1905679. [[CrossRef](#)] [[PubMed](#)]
48. Konopatsky, A.S.; Firestein, K.L.; Leybo, D.V.; Sukhanova, E.V.; Popov, Z.I.; Fang, X.; Manakhov, A.M.; Kovalskii, A.M.; Matveev, A.T.; Shtansky, D.V.; et al. Structural evolution of Ag/BN hybrids via a polyol-assisted fabrication process and their catalytic activity in CO oxidation. *Catal. Sci. Technol.* **2019**, *9*, 6460–6470. [[CrossRef](#)]
49. Xie, Y.H.; Liu, B.L.; Li, Y.Z.; Chen, Z.X.; Cao, Y.L.; Jia, D.Z. Cu/Cu<sub>2</sub>O/rGO nanocomposites: Solid-state self-reduction synthesis and catalytic activity for p-nitrophenol reduction. *New J. Chem.* **2019**, *43*, 12118–12125. [[CrossRef](#)]
50. Rong, Y.; Cao, Y.; Guo, N.; Li, Y.; Jia, W.; Jia, D. A simple method to synthesize V<sub>2</sub>O<sub>5</sub> nanostructures with controllable morphology for high performance Li-ion batteries. *Electrochim. Acta* **2016**, *222*, 1691–1699. [[CrossRef](#)]
51. Xie, J.; Cao, Y.; Jia, D.; Li, Y.; Wang, K.; Xu, H. In situ solid-state fabrication of hybrid AgCl/AgI/AgIO<sub>3</sub> with improved UV-to-visible photocatalytic performance. *Sci. Rep.* **2017**, *7*, 12365. [[CrossRef](#)]
52. Wang, Q.; Ming, M.; Niu, S.; Zhang, Y.; Fan, G.Y.; Hu, J.S. Scalable solid-state synthesis of highly dispersed uncapped metal (Rh, Ru, Ir) nanoparticles for efficient hydrogen evolution. *Adv. Energy Mater.* **2018**, *8*, 1801698. [[CrossRef](#)]
53. Xiong, H.; Zhou, H.; Sun, G.; Liu, Z.; Zhang, L.; Zhang, L.; Du, F.; Qiao, Z.; Dai, S. Solvent-free self-assembly for scalable preparation of highly crystalline mesoporous metal oxides. *Angew. Chem. Int. Ed.* **2020**, *59*, 11053–11060. [[CrossRef](#)]
54. Chawla, S.K.; Sankarraman, N.; Payer, J.H. Diagnostic spectra for XPS analysis of Cu-O-S-H compounds. *J. Electron. Spectrosc.* **1992**, *61*, 1–18. [[CrossRef](#)]
55. Rastegarpanah, A.; Rezaei, M.; Meshkani, F.; Dai, H. 3D ordered honeycomb-shaped CuO·Mn<sub>2</sub>O<sub>3</sub>: Highly active catalysts for CO oxidation. *Mol. Catal.* **2020**, *485*, 110820. [[CrossRef](#)]
56. Chang, H.-W.; Chen, S.-C.; Chen, P.-W.; Liu, F.-J.; Tsai, Y.-C. Constructing morphologically tunable copper oxide-based nanomaterials on Cu wire with/without the deposition of manganese oxide as bifunctional materials for glucose sensing and supercapacitors. *Int. J. Mol. Sci.* **2022**, *23*, 3299. [[CrossRef](#)]
57. Liu, B.; Cao, Y.; Zhang, H.; Wang, S.; Geng, Q.; Li, Y.; Dong, F. Constructing ultrafine Cu nanoparticles encapsulated by N-doped carbon nanosheets with fast kinetics for high-performance lithium/sodium storage. *Chem. Eng. J.* **2022**, *446*, 136918. [[CrossRef](#)]
58. Skinner, W.M.; Prestidge, C.A.; Smart, R.S.C. Irradiation effects during XPS studies of Cu(II) activation of zinc sulphide. *Surf. Interface Anal.* **1996**, *24*, 620–626. [[CrossRef](#)]
59. Qian, K.; Qian, Z.; Hua, Q.; Jiang, Z.; Huang, W. Structure–activity relationship of CuO/MnO<sub>2</sub> catalysts in CO oxidation. *Appl. Surf. Sci.* **2013**, *273*, 357–363. [[CrossRef](#)]
60. Xu, X.L.; Li, L.; Huang, J.; Jin, H.; Fang, X.Z.; Liu, W.M.; Zhang, N.; Wang, H.M.; Wang, X. Engineering Ni<sup>3+</sup> cations in NiO lattice at the atomic level by Li<sup>+</sup> doping: The roles of Ni<sup>3+</sup> and oxygen species for CO oxidation. *ACS Catal.* **2018**, *8*, 8033–8045. [[CrossRef](#)]
61. Wang, X.Y.; Li, X.Y.; Mu, J.C.; Fan, S.Y.; Chen, X.; Wang, L.; Yin, Z.F.; Tade, M.; Liu, S.M. Oxygen vacancy-rich porous Co<sub>3</sub>O<sub>4</sub> nanosheets toward boosted NO reduction by CO and CO oxidation: Insights into the structure-activity relationship and performance enhancement mechanism. *ACS Appl. Mater. Interfaces* **2019**, *11*, 41988–41999. [[CrossRef](#)] [[PubMed](#)]
62. Liu, B.; Li, Y.; Wu, H.; Ma, F.; Cao, Y. Room-temperature solid-state preparation of CoFe<sub>2</sub>O<sub>4</sub>@Coal composites and their catalytic performance in direct coal liquefaction. *Catalysts* **2020**, *10*, 503. [[CrossRef](#)]
63. Mo, S.P.; Zhang, Q.; Li, J.; Sun, Y.H.; Ren, Q.M.; Zou, S.B.; Zhang, Q.; Lu, J.H.; Fu, M.L. Highly efficient mesoporous MnO<sub>2</sub> catalysts for the total toluene oxidation: Oxygen-vacancy defect engineering and involved intermediates using in situ DRIFTS. *Appl. Catal. B Environ.* **2020**, *264*, 1184641–11846416. [[CrossRef](#)]

64. Zou, Q.; Zhao, Y.; Jin, X.; Fang, J.; Li, D.; Li, K.; Lu, J.; Luo, Y. Ceria-nano supported copper ox-ide catalysts for CO preferential oxidation: Importance of oxygen species and metal-support inter-action. *Appl. Surf. Sci.* **2019**, *494*, 1166–1176. [[CrossRef](#)]
65. Wu, P.; Dai, S.Q.; Chen, G.X.; Zhao, S.Q.; Xu, Z.; Fu, M.L.; Chen, P.R.; Chen, Q.; Jin, X.J.; Qiu, Y.C.; et al. Interfacial effects in hierarchically porous  $\alpha$ -MnO<sub>2</sub>/Mn<sub>3</sub>O<sub>4</sub> heterostruc-tures promote photocatalytic oxidation activity. *Appl. Catal. B Environ.* **2019**, *268*, 118418. [[CrossRef](#)]
66. Lin, J.; Guo, Y.; Chen, X.; Li, C.; Lu, S.; Liew, K.M. CO Oxidation over Nanostructured Ceria Supported Bimetallic Cu-Mn Oxides Catalysts: Effect of Cu/Mn Ratio and Calcination Temperature. *Catal. Lett.* **2018**, *148*, 181–193. [[CrossRef](#)]
67. Zhou, Y.; Liu, X.; Wang, K.; Li, J.; Zhang, X.; Jin, X.; Tang, X.; Zhu, X.; Zhang, R.; Jiang, X.; et al. Porous Cu-Mn-O catalysts fabricated by spray pyrolysis method for efficient CO oxidation. *Results Phys.* **2019**, *12*, 1893–1900. [[CrossRef](#)]
68. Choi, K.-H.; Lee, D.-H.; Kim, H.-S.; Yoon, Y.-C.; Park, C.-S.; Kim, Y.H. Reaction Characteristics of Precious-Metal-Free Ternary Mn-Cu-M (M = Ce, Co, Cr, and Fe) Oxide Catalysts for Low-Temperature CO Oxidation. *Ind. Eng. Chem. Res.* **2016**, *55*, 4443–4450. [[CrossRef](#)]